This document collects supporting figures referenced in the main text. Figures S1-S5 provide the integral curve visualization and sample density (S1, S2), the detailed second-order gradient response (S3), the two panel structural correspondence between descriptive levels (S4), and the full nine-configuration robustness study of the inverse-square zero distance law (S5). All quantities are evaluated from the closed form expressions and analytic derivatives of the exact counter-propagating rational pulse state defined in the main text, with the same dimensionless units $c = \hbar = 1$.

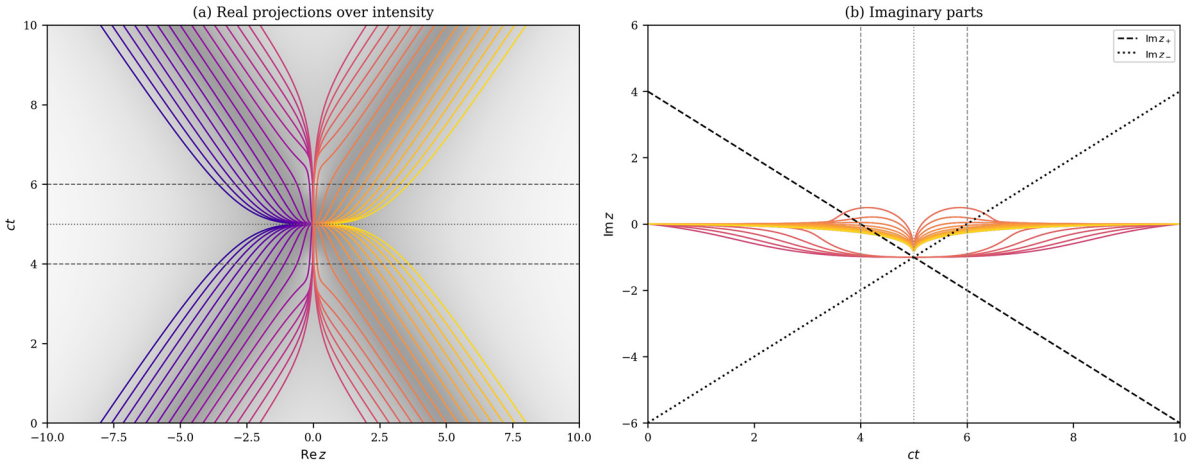


Figure S1. Complex integral curves generated by$\chi = -c^2\psi_x/\psi_t$ on the two regular time intervals. The pre-collision curves are seeded at $ct = 0$ and integrated forward; the independent post-collision curves are seeded at $ct = 10$ and integrated backward. (a) Real projections over the intensity background. (b) Imaginary parts; dashed lines show the analytic Im($z_\pm$). The two ensembles resolve the zero crossings at $ct = x_0 - \ell$ and $ct = x_0 + \ell$ without continuing through the globally singular $\psi_t = 0$ slice at $ct = x_0$.

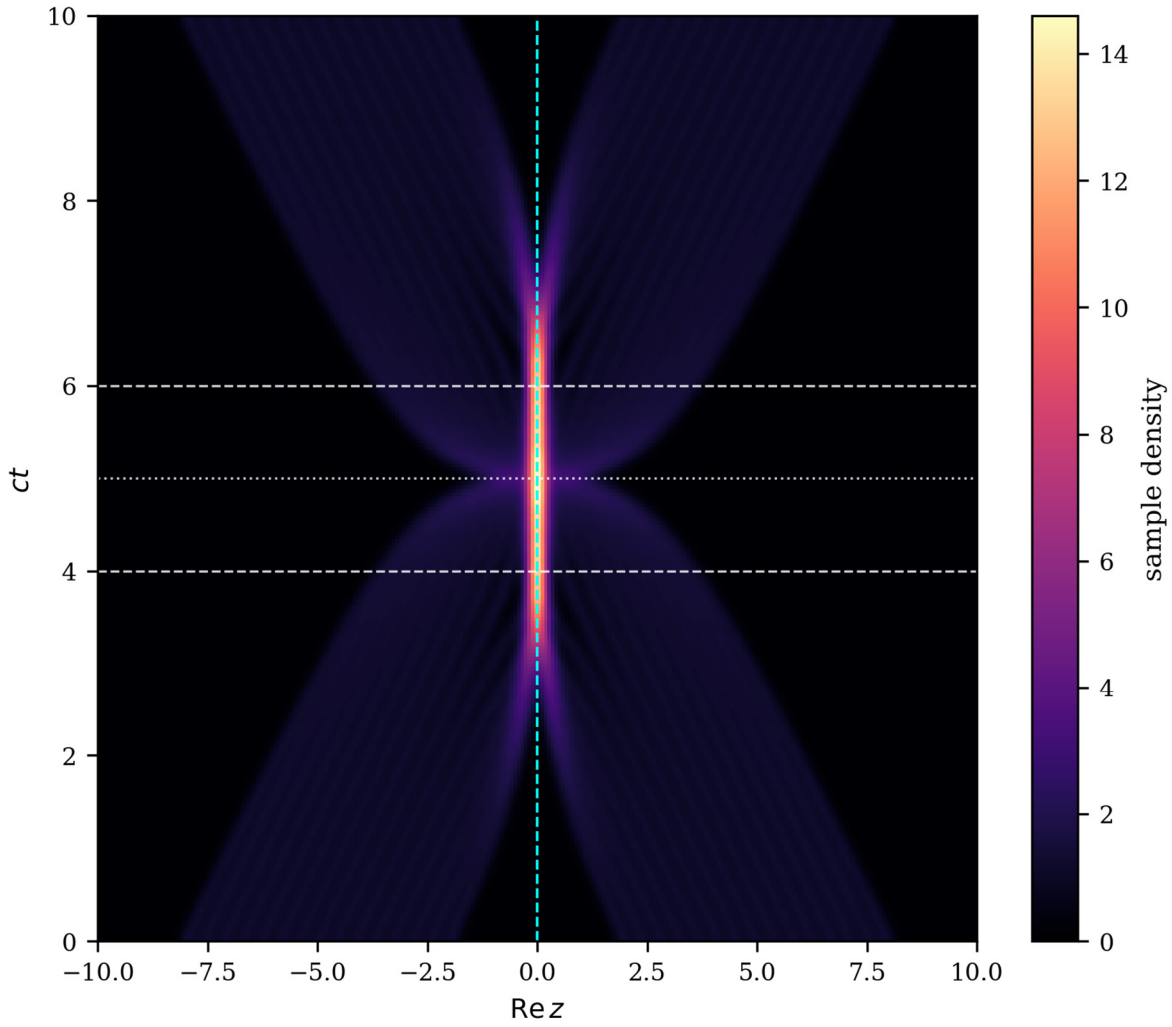


Figure S2. Smoothed sample density of the real projections of the pre- and post-collision integral curve ensembles. The density is symmetric about $ct = x_0$ and concentrates near the two zero crossing events at $ct = x_0 \mp \ell$. It is a geometric descriptor of the sampled integral curves, not a probability distribution.

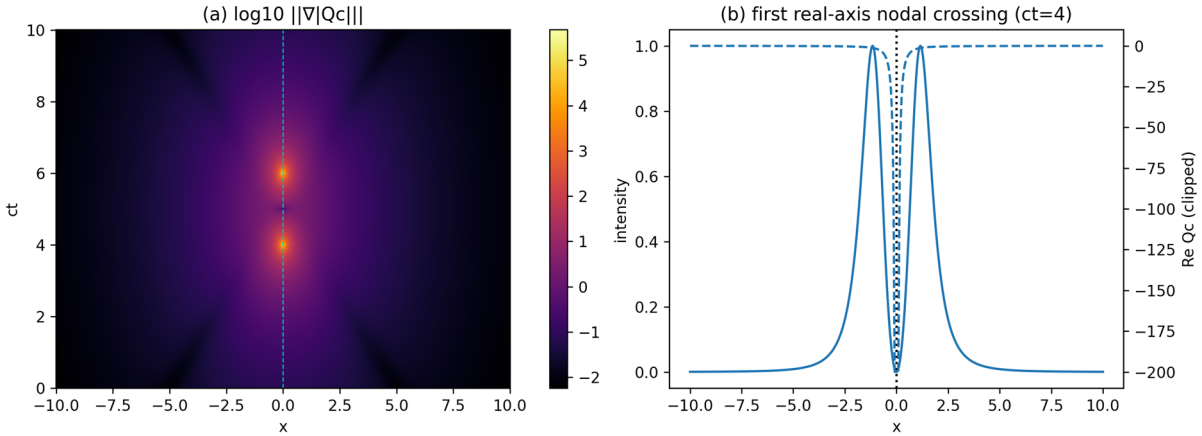


Figure S3. Localization of the second-order response near the real axis interference zeros. (a) log_{10} of the gradient magnitude associated with Q_c in the (x, ct) plane. The strongest gradients are localized near the two real axis zero crossings at $ct = 4$ and $ct = 6$. (b) Real axis profile at the first zero crossing, $ct = 4$. The field intensity vanishes at

$x = 0$, coincident with the singular excursion of $\mathrm{Re}(Q_c)$(shown with clipping for visualization).

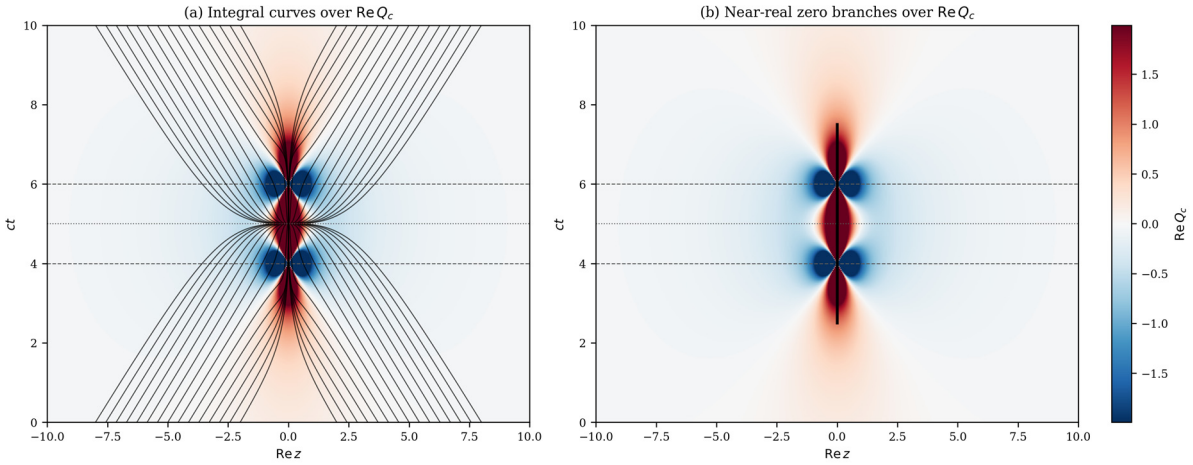


Figure S4. Structural correspondence across the descriptive levels. (a) Real projections of the transport integral curves over $\mathrm{Re}(Q_c)$. (b) Near real portions of the exact zero branches over $\mathrm{Re}(Q_c)$. The compact second-order lobes and strongest finite redistribution of the integral curves occupy the same zero selected domains.

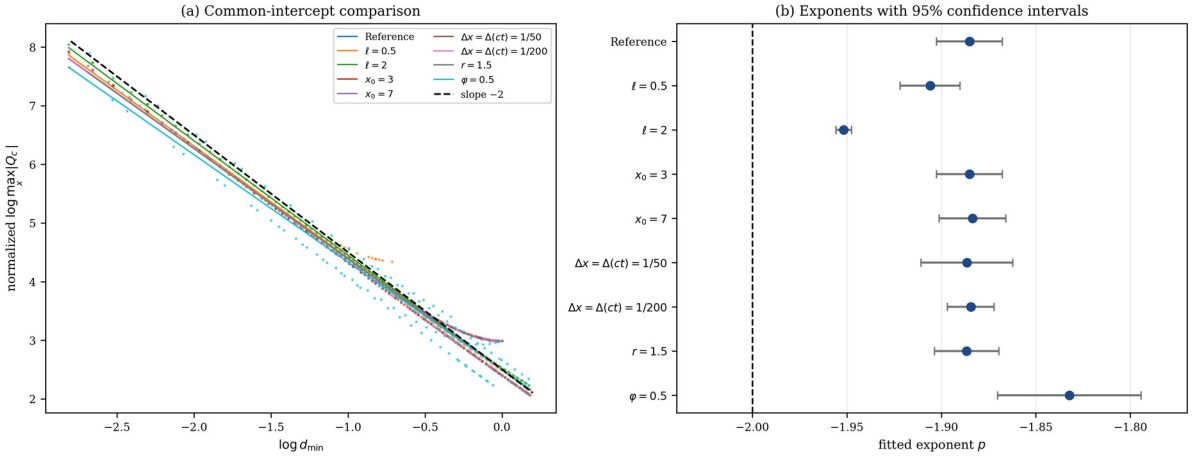


Figure S5. Robustness of the inverse square zero distance law within the tested second-order rational pulse family. (a) Log-log data for the nine configurations of Table 2 (main text), each shifted to its fitted intercept; the dashed reference has a slope of -2. (b) Individual exponents with 95% confidence intervals. The colors distinguish the width, separation, coupled grid, and asymmetric variations.

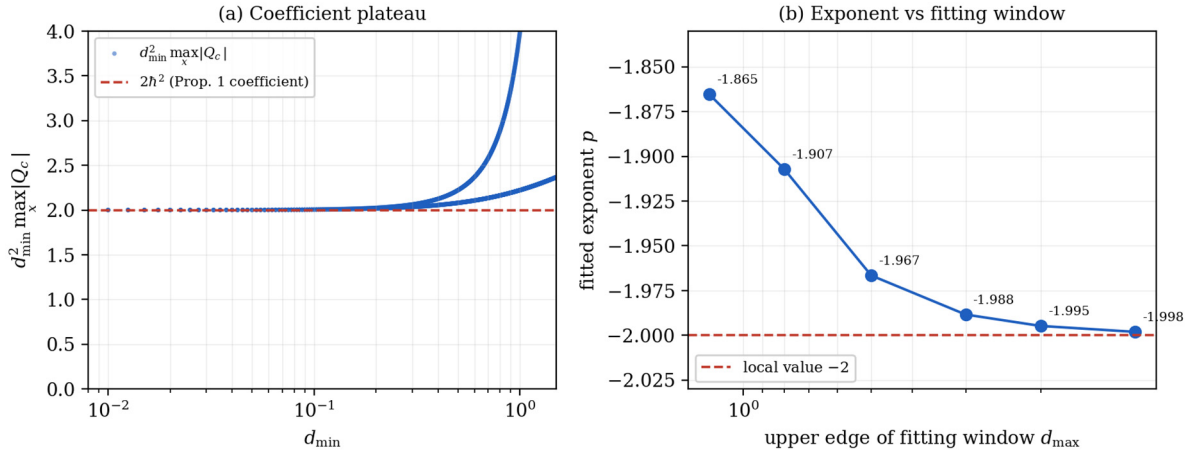


Figure S6. Direct verification of the inverse-square coefficient for the symmetric reference state ($r = 1, \varphi = 0$). (a) The compensated quantity $d^2_{\min} \cdot \max_x |Q_c|$ approaches the constant $2\hbar^2$ predicted by the local expansion (Eq. (28) of the main text) as $d_{\min} \to 0$; the rise above the plateau at larger $d_{\min}$ reflects the second interference zero and higher-order terms. (b) The exponent obtained by fitting $\max_x |Q_c| \propto d^p_{\min}$ over progressively narrower distance windows converge monotonically to the local value −2 as the upper edge $d_{\max}$ of the window is reduced (Table 3 of the main text). Grid $\Delta x = \Delta(ct) = 1/200$, $|\psi| \geq 2 \times 10^{-3}$ mask.